Journal of Materials Chemistry A

ROYAL SOCIETY OF CHEMISTRY

PAPER

View Article Online
View Journal

Cite this: DOI: 10.1039/d5ta09970f

From lithium to proton mobility in garnet electrolytes: an NMR and conductivity study of $H_{5.2}Li_{1.3}La_3Zr_{1.5}Ta_{0.5}O_{12}$

Florian Stainer, [a] Junji Akimoto, [b] Yoshitaka Matsushita, [b] Kazutaka Mitsuishi, [b] Kazunori Takada [b] and H. Martin R. Wilkening *[a]

Garnet-type oxides are among the most promising solid-state electrolytes owing to their high chemical stability and comparatively high lithium-ion conductivity. They may also provide a basis for proton conductors through Li^+/H^+ exchange. In a recent ^1H and ^7Li NMR study, we showed that minor proton incorporation in single-crystalline garnets exerts only a weak influence on Li-ion diffusion. Here, we investigate the polycrystalline hydrogarnet $H_{5.2}Li_{1.3}La_3Zr_{1.5}Ta_{0.5}O_{12}$ (HLZTO), obtained by aqueous Li^+/H^+ exchange from $Li_{6.5}La_3Zr_{1.5}Ta_{0.5}O_{12}$ (LLZTO). The precursor, synthesised at the remarkably low temperature of 600 °C, exhibits a large surface area enabling an efficient exchange process. X-ray diffraction reveals a slight lattice expansion upon protonation, while ^6Li high-resolution MAS NMR and Raman spectroscopy indicate a pronounced alteration of the local Li environment. Thermogravimetric analysis shows a 5.5 wt% loss between 200 and 600 °C, consistent with the release of H_2O. The total ionic conductivity of LLZTO is constrained by poor interparticle contact, whereas in HLZTO it drops sharply upon heating as protons are removed. Variable-temperature ^1H NMR relaxation reveals a diffusion-induced maximum between 125 and 180 °C, resulting in a self-diffusion coefficient $D \approx 1 \times 10^{-15}$ m^2 s^{-1} (*ca.* 150 °C). As seen by ^7Li NMR, the remaining Li ions in HLZTO are almost immobile on the NMR time scale, revealing that proton motion dominates charge transport in HLZTO. While defects in LLZO promote localized motions, their healing appears to facilitate the establishment of long-range Li^+ transport pathways.

Received 5th December 2025
Accepted 14th April 2026

DOI: 10.1039/d5ta09970f

rsc.li/materials-a

Introduction

Proton-conducting ceramics have attracted growing attention as key materials for next-generation electrochemical energy devices. Their appeal stems from the fact that proton diffusion typically involves a lower activation energy than, *e.g.*, oxygen-ion diffusion, allowing high ionic conductivities to be achieved at considerably lower temperatures.[1] Over the past decades, a wide variety of ceramic proton conductors has been developed for solid oxide fuel cells, electrolysers, and related applications.[2–5] Among them, certain inorganic proton conductors such as $CsHSO_4$ (ref. 6) and $CsOH \cdot H_2O$[7] exhibit high proton conductivities but tend to undergo deprotonation or melting at temperatures near 200 °C. Perovskite-type oxides, including $SrCeO_3$,[8] co-doped $BaZrO_3$,[9–11] and $BaCeO_3$ (ref. 12) display much greater thermal stability, yet still require operation above 400 °C to reach significant conductivities. Consequently, considerable research efforts have focused on identifying new materials that support fast proton transport in the intermediate-temperature regime. A particularly promising direction involves lithium/proton-exchanged lithium conductors, such as the lithium superionic conductor $Li_{13.9}Sr_{0.1}Zn(GeO_4)_4$ (ref. 13) and the garnet-type $Li_7La_3Zr_2O_{12}$.[14–16]

Another route toward proton incorporation in garnets emerged from studies on their chemical instability under humid conditions. It was shown that in ambient air, the garnet $Li_7La_3Sn_2O_{12}$ undergoes spontaneous partial protonation, while the released lithium reacts with CO_2 to form Li_2CO_3.[17] To avoid carbonate formation, several researchers have instead employed controlled Li^+/H^+ exchange reactions using benzoic acid,[17,18] acetic acid,[18,19] or even water.[20] Over the past decade, a variety of techniques has been applied to probe proton transport in such systems. Howard *et al.* reported that in Ga-substituted $Li_7La_3Zr_2O_{12}$, the bulk ionic conductivity measured under wet N_2 decreased, while the grain boundary resistance was simultaneously reduced.[21] Truong *et al.* observed an enhanced conductivity ($\sim 10^{-5}$ S cm^{-1}) in $Li_5La_3Nb_2O_{12}$ using acid-treated Nafion and Pt–C electrodes under wet N_2, confirming that neither electrons nor oxide ions contributed to

[a]Graz University of Technology, Institute of Chemistry and Technology of Materials (NAWI Graz), Stremayrgasse 9, 8010 Graz, Austria. E-mail: wilkening@tugraz.at; stainer@tugraz.at

[b]National Institute for Materials Science (NIMS), Tskuba, Ibaraki 305-0044, Japan. E-mail: akimoto.junji@nims.go.jp; matsushita.yoshitaka@nims.go.jp; mitsuishi.kazutaka@nims.go.jp; takada.kazunori@nims.go.jp

the total conductivity.[22] However, these studies could not separate the individual contributions of Li^+ and H^+, highlighting the need for local probes such as solid-state nuclear magnetic resonance (NMR) spectroscopy.

Subsequent investigations have characterised proton diffusivity in garnets by various methods. Hiebl *et al.* determined a diffusion coefficient D of $\sim 10^{-17}$ m^2 s^{-1} in Al-stabilised $Li_7La_3Zr_2O_{12}$ single crystals using X-ray diffraction (XRD).[23] For polycrystalline Ga-stabilised $Li_7La_3Zr_2O_{12}$, Smetaczek *et al.* obtained $D \approx 7 \times 10^{-17}$ m^2 s^{-1} at 80 °C by laser-induced breakdown spectroscopy,[24] while Brugge *et al.* reported a similar diffusivity ($\sim 10^{-16}$ m^2 s^{-1} at 100 °C) using secondary ion mass spectrometry.[25] Recently, we demonstrated for single-crystalline $Li_6La_3ZrTaO_{12}$ that low proton concentrations introduced *via* Li^+/H^+ exchange only slightly reduce lithium-ion mobility, as shown by ^7Li spin-lattice relaxation (SLR) NMR.[19] Complementary ^1H NMR measurements revealed that these protons are also mobile with a self-diffusion coefficient of $D \approx 1.2 \times 10^{-15}$ m^2 s^{-1} at 125 °C, albeit less so than Li^+. Furthermore, we showed that at lower temperatures, proton spin relaxation is influenced by the spin fluctuations of the faster-diffusing lithium ions.

In the present study, we investigate the diffusion properties of a polycrystalline lithium/proton-exchanged garnet. The precursor $Li_{6.5}La_3Zr_{1.5}Ta_{0.5}O_{12}$ (LLZTO) was synthesised from a mixture of Li_2O and fluorite-type $La_3Zr_{1.5}Ta_{0.5}O_{8.75}$ using a soft-sintering process at only 600 °C, significantly lower than the >1000 °C typically required for conventional garnet synthesis. This low-temperature route yielded a material with a comparatively large surface area, which facilitated efficient Li^+/H^+ exchange in water at mildly elevated temperatures. The extent of proton exchange was quantified by inductively coupled plasma optical emission spectroscopy (ICP-OES) and thermogravimetric calorimetry (TGA).

After the ion-exchange reaction, the material retained its cubic structure but exhibited a slightly expanded lattice parameter. Fig. 1 shows the crystal structure of $Li_{6.5}La_3Zr_{1.5}Ta_{0.5}O_{12}$, obtained from single-crystal measurements, including the Li-site occupancies determined by neutron diffraction.[26] In

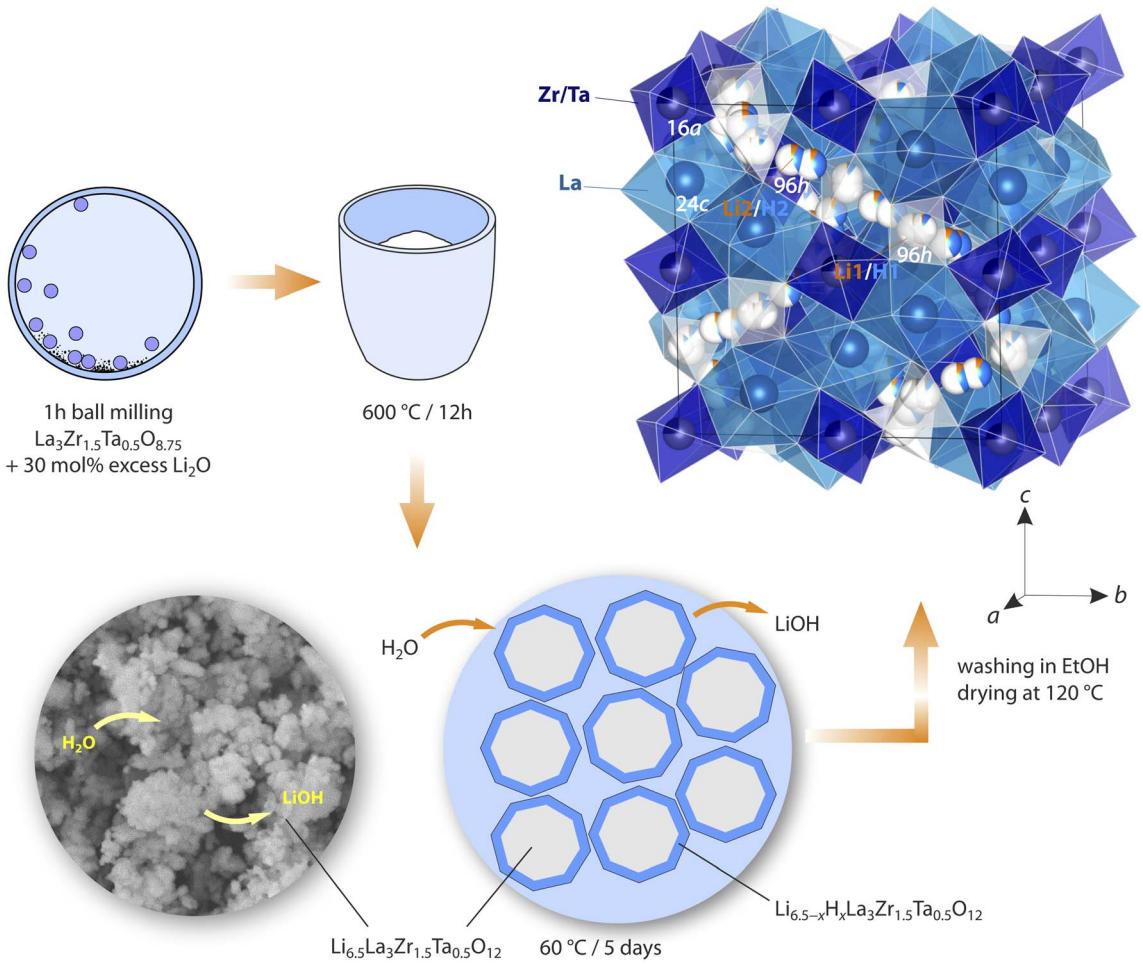

Fig. 1 Scheme illustrating the preparation steps to obtain the hydrogarnet. Cubic crystal structure (space group *Ia*-3*d*) of H-bearing $Li_{6.5}La_3Zr_{1.5}Ta_{0.5}O_{12}$; the structure is based on that of single-crystalline $Li_{6.5}La_3Zr_{1.5}Ta_{0.5}O_{12}$ taken from the ICSD (collection code: 22957).[26] The framework consists of corner-sharing ZrO_6/TaO_6 octahedra (16*a* sites) and La^{3+} cations occupying the 24*c* positions. Lithium ions form a highly disordered substructure distributed over two crystallographically distinct sites, both located on 96*h*: Li_1 arises from a split octahedral 48*g* position (42% occupancy), whereas Li_2 corresponds to a split tetrahedral 24*d* site (12% occupancy). The partial occupancies reflect the intrinsic disorder characteristic of garnet-type Li conductors. Oxygen atoms are omitted for clarity.

our previous work, we demonstrated that at low proton concentrations, protons preferentially replace Li^+ ions on the less-occupied octahedral sites.[19] At higher exchange levels, however, occupation of all Li sites becomes increasingly likely. Furthermore, in materials with high surface areas, protons may also participate in diffusion processes along grain boundaries, as reported for various oxides,[27] and such behaviour can be anticipated for the present system as well.

The aim of this study is to investigate the proton and lithium dynamics in both the polycrystalline garnet precursor LLZTO and the corresponding hydrogarnet (see below, denotes as HLZTO) over long-range and local length scales. To this end, we employed ^{7}Li and ^{1}H SLR NMR spectroscopy and conductivity spectroscopy to probe ion transport across different spatial and dynamic regimes. In addition, Raman spectroscopy and ^{6}Li magic-angle spinning (MAS) NMR were used to elucidate changes in the local environment of lithium ions between LLZTO and the hydrogarnet.

Experimental

Preparation of the lithium-bearing garnet samples

Polycrystalline $Li_{6.5}La_3Zr_{1.5}Ta_{0.5}O_{12}$ (LLZTO) was prepared by reacting Li_2O with fluorite-type $La_3Zr_{1.5}Ta_{0.5}O_{8.75}$ at 600 °C, as recently reported.[28–30] $La_3Zr_{1.5}Ta_{0.5}O_{8.75}$ was first synthesised by a polymerised complex method. The educts $La(NO_3)_3\cdot 6H_2O$ (Fujifilm Wako Pure Chemical Industries, 99.9%), $TaCl_5$ (Rare Metallic Co., Ltd, 99.9%), and $ZrOCl_2\cdot 8H_2O$ (Fujifilm Wako Pure Chemical Industries, 99.9%) were dissolved in dehydrated ethanol at room temperature in a stoichiometric molar ratio of La : Zr : Ta = 6 : 3 : 1. Ethylene glycol (Fujifilm Wako Pure Chemical Industries, 99.9%) and citric acid (Fujifilm Wako Pure Chemical Industries, 95%) were then added, and the solution was stirred at 70 °C for 5 h and subsequently dried at 200 °C for 12 h. The resulting mixture was heated in a mantle heater at 350 °C for 2 h, followed by calcination in an electric furnace at 1000 °C for 12 h in air.

LLZTO powder samples were prepared from Li_2O (Kojundo Chemical Laboratory, 99%) and the precursor $La_3Zr_{1.5}Ta_{0.5}O_{8.75}$. The precursor oxide was mixed with a 30 mol% excess of Li_2O and ball-milled for 1 h in a zirconia vessel filled with Ar gas. The mixture obtained was then heated at 600 °C for 12 h in alumina crucibles under flowing argon gas atmosphere.

$$3.25\ Li_2O + La_3Zr_{1.5}Ta_{0.5}O_{8.75} \rightarrow Li_{6.5}La_3Zr_{1.5}Ta_{0.5}O_{12} \quad (1)$$

Preparation of protonated samples *via* ion exchange

The protonated, polycrystalline garnet $H_{6.5-x}Li_xLa_3Zr_{1.5}Ta_{0.5}O_{12}$ was obtained by Li^+/H^+ ion exchange of LLZTO powder in water at 60 °C for 5 days.

$$Li_{6.5}La_3Zr_{1.5}Ta_{0.5}O_{12} + (6.5 - x)\ H_2O \rightarrow H_{6.5-x}Li_xLa_3Zr_{1.5}Ta_{0.5}O_{12} + (6.5 - x)\ LiOH \quad (2)$$

The solution was refreshed daily, and the progress of the ion-exchange reaction was monitored *via* the pH of the solution. After completion, the sample was washed with ethanol and dried under vacuum at 120 °C.

Characterization of structure, composition and morphology

The powder samples were characterised in air by powder XRD using a Rigaku SmartLab3 diffractometer equipped with a D/teX Ultra250 one-dimensional detector and operating with monochromatised Cu K_α radiation ($\lambda = 1.54187$ Å, 40 kV, 30 mA). XRD patterns were collected over a 2θ range of 5 to 140° with a step size of 0.02° and a scan speed of 1.0° min^{-1}. Lattice parameters and crystal structures of the samples were refined using the Jana2020 program.[31] To investigate structural changes in the protonated garnet upon heating, X-ray diffraction was performed on a Rigaku Miniflex 600 diffractometer equipped with a benchtop heating stage (BTS 500, Anton Paar) over the temperature range 30 to 300 °C. The diffractograms were recorded with Cu K_α radiation over a 2θ range of 8 to 90° with a step size of 0.01° and a scan speed of 5.0° min^{-1}. The particle size and morphology were analysed by scanning electron microscopy (SEM, Hitachi FlexSEM 1000 II).

The residual Li content was determined by ICP-OES (Agilent 5800). To evaluate the hydrogen content and thermal stability of the protonated garnet sample up to 1000 °C in air, thermogravimetric and differential thermal analysis (TG-DTA) was performed using a Rigaku (TG-DTA8122) instrument with heating and cooling rates of 10 °C min^{-1} and a 1 h hold at 1000 °C.

Nuclear spin relaxation

NMR experiments were performed on a Bruker Avance III spectrometer equipped with an ultrashielded 300 MHz wide-bore magnet operating at a nominal field of 7 T. This corresponds to Larmor frequencies of $\omega_0/2\pi = 116$ MHz for ^{7}Li and 300 MHz for ^{1}H. ^{7}Li NMR spectra were recorded using single-pulse excitation with a 90° pulse length of 2.6 μs and a radio-frequency power of 200 W; 16 scans were accumulated for each spectrum. For ^{1}H NMR, pulse lengths of 1.1 to 1.7 μs (depending on temperature) and a power of 200 W were used, with 4 scans collected per spectrum. All spectra were obtained by Fourier transformation of the free induction decays (FIDs) without further processing.

^{1}H and ^{7}Li NMR SLR rates in the laboratory frame of reference ($1/T_1$) were measured using the saturation recovery pulse sequence (see Epp *et al.*[32]). In this sequence, a train of 10 closely spaced 90° pulses destroys any longitudinal magnetization M_z. The recovery of M_z was then recorded as a function of the variable waiting time t_d using a 90° detection pulse. The time integral of the FIDs was used to construct the magnetization curves $M(t_d)$, which were parameterised with stretched exponentials: $M_z(t_d) \propto 1 - \exp(-(t_d/T_1(T))^\gamma)$. The stretching factor γ varied between 0.4 and 1 depending on temperature. The corresponding SLR rates in the rotating frame ($1/T_{1\rho}$) were obtained using the spin-locking method. A locking field corresponding to 20 kHz was applied for both ^{1}H and ^{7}Li NMR measurements, which locks the spin precession in the $(x - y)'$-plane after the excitation pulse. The decaying magnetization along the y'-axis, $M_y(t_{lock})$, was recorded as a function of variable locking pulse times and analysed with

stretched exponentials: $M_y(t_{lock}) \propto \exp(-(t_{lock}/T_{1\rho}(T))^{\gamma})$. Here, we obtained γ values ranging from 0.3 to 1 depending on temperature. Unless stated otherwise, SLR measurements were performed over the temperature range from −95 to 260 °C. Prior to the measurements, samples were fire-sealed under vacuum in Duran glass tubes (4 cm length, 3 mm inner diameter) to prevent any reaction with oxygen or moisture. Sample temperature was monitored in close proximity and controlled *via* a stream of heated nitrogen gas.

^{6}Li and ^{1}H MAS NMR

^{6}Li MAS NMR spectra were acquired on a Bruker Avance III 500 spectrometer equipped with an ultrashielded 500 MHz wide-bore magnet (11.74 T), corresponding to resonance frequencies of 73.6 MHz for ^{6}Li and 500 MHz for ^{1}H. Chemical shifts were referenced to ^{6}Li in $CH_3COOLi\cdot(H_2O)_x$ and to the ^{1}H resonance of adamantane, respectively. All measurements were performed at spinning speeds of 22 or 25 kHz and a bearing gas temperature of 303 K. ^{6}Li spectra were obtained using a single $\pi/2$ pulse of 2.4 μs at 100 W, accumulating 500 scans with a recycle delay of 10 s. ^{1}H spectra were recorded with a $\pi/2$ pulse of 0.8 μs at 20 W, accumulating 16 scans with a 3 s delay between scans. The powdered samples were packed under an argon atmosphere into 2.5 mm ZrO_2 rotors fitted with Vespel caps.

Raman spectroscopy

Raman spectra were recorded using a Thermo Fisher DXR Raman microscope equipped with a 532 nm, 5 mW laser. The powdered samples were loaded into glass capillaries with a 4 mm diameter, and spectra were collected over the range 40 to 3500 cm^{-1}.

Conductivity measurements

Pellets with a diameter of 5 mm were prepared by pressing the powder samples at 260 MPa and subsequently coating both sides with a Li-blocking Au layer (≈50 nm) using a sputter coater (Leica SCD050). These pellets, with an estimated density above 85%, were used for alternating-current conductivity measurements. The sample LLZTO500 was soft-sintered *ex situ* at 500 °C for 12 h inside an argon-filled glovebox prior to measurement.

Conductivity data were recorded using a Novocontrol Concept 80 broadband dielectric spectrometer equipped with an Alpha-A analyzer and an active ZGS sample cell (Novocontrol). The sputtered pellets were stored and measured under argon using an airtight in-house fabricated sample holder made of Teflon with brass contacts. Electrical contact between the pellet and the sample cell was ensured *via* secondary brass electrodes and a spring washer.

Conductivity measurements typically consisted of a heating run (20 °C to 260 °C) followed by a cooling run (260 °C to −100 °C) in 20 °C steps. The temperature inside the impedance cell was controlled by heated nitrogen gas supplied through a QUATRO cryo-system (Novocontrol). For high-temperature measurements up to 600 °C, a Novotherm-HT system (Novocontrol) equipped with a tube furnace and a ceramic sample cell with platinum electrodes was used. In this setup, the pellet was clamped between the electrodes using multiple springs and maintained under a constant nitrogen gas flow during measurement. The frequency range covered was 0.05 Hz to 10 MHz.

Results

Synthesis and structural details of the proton exchanged garnet

The precursor LLZTO ($Li_{6.5}La_3Zr_{1.5}Ta_{0.5}O_{12}$) was successfully synthesised from $La_{2.4}Zr_{1.2}Ta_{0.4}O_7$ and Li_2O, as described above. The LLZTO powder exhibits submicrometer-sized particles (Fig. S1), as confirmed by SEM. To achieve a high degree of Li^+/H^+ exchange, the LLZTO powder was immersed in water at 60 °C for 5 days, yielding the proton-exchanged garnet. The highly porous morphology of LLZTO facilitated the exchange process, while the submicrometer particle size was preserved after proton exchange (Fig. S1).

Energy-dispersive X-ray spectroscopy (EDX) elemental mapping confirmed a homogeneous distribution of La, Zr, and Ta across the hydrogarnet particles (see Fig. S2). Elemental analysis by EDX yielded a composition of 20.6 at% La, 10.6 at% Zr, 2.4 at% Ta, and 66.3 at% O. Transmission electron microscopy (TEM) images revealed particle sizes in the range of 100 to 300 nm, consistent with the SEM observations. Nanobeam diffraction TEM analysis confirmed that the particles are crystalline and free of amorphous regions.

An ICP-OES analysis of the hydrogarnet yielded a metal ratio of Li : La : Zr : Ta = 1.30 : 3 : 1.50 : 0.50, in good agreement with the values obtained from EDX. The proton content was determined from TG-DTA measurements. As shown in Fig. 2a, the TGA curve displays two distinct weight-loss steps: a minor loss of 0.29 wt% between 25 and 200 °C, attributed to adsorbed water, and a more pronounced loss of 5.50 wt% between 200 and 600 °C, corresponding to dehydration of the compound itself. This latter value agrees well with the theoretical weight loss (5.54 wt%) expected for 5.2 protons per formula unit released as H_2O. Accordingly, the chemical composition of the protonated powder sample was estimated as $H_{5.20}Li_{1.30}La_3Zr_{1.5}Ta_{0.5}O_{12}$ (hereafter referred to as HLZTO), based on the combined results from optical emission spectroscopy and TG-DTA analysis. The signal at 733 °C in DTA might be ascribed to the melting of Li_2CO_3 present in the sample, see below.

Fig. 2b shows the XRD patterns of the LLZTO and HLZTO samples. All reflections can be indexed to the cubic garnet-type structure. The cubic lattice parameter of the LLZTO sample, refined by the Le Bail method,[31] was $a = 12.95767(10)$ Å, in good agreement with previously reported values.[28–30] For the HLZTO sample, the cubic lattice parameter was determined to be $a = 13.04605(7)$ Å, which is larger than that reported for a partially proton-exchanged sample, $Li_{3.72}H_{2.78}La_3Zr_{1.5}Ta_{0.5}O_{12}$ sample ($a = 13.0049$ Å).[33] This pronounced lattice expansion indicates that the Li^+/H^+ exchange reaction proceeded further in the present study, likely facilitated by the fine particle morphology and large specific surface area of the powders.

In addition, an extra reflection at $2\theta = 21.5°$, corresponding to the (310) plane, was observed in the XRD pattern. The

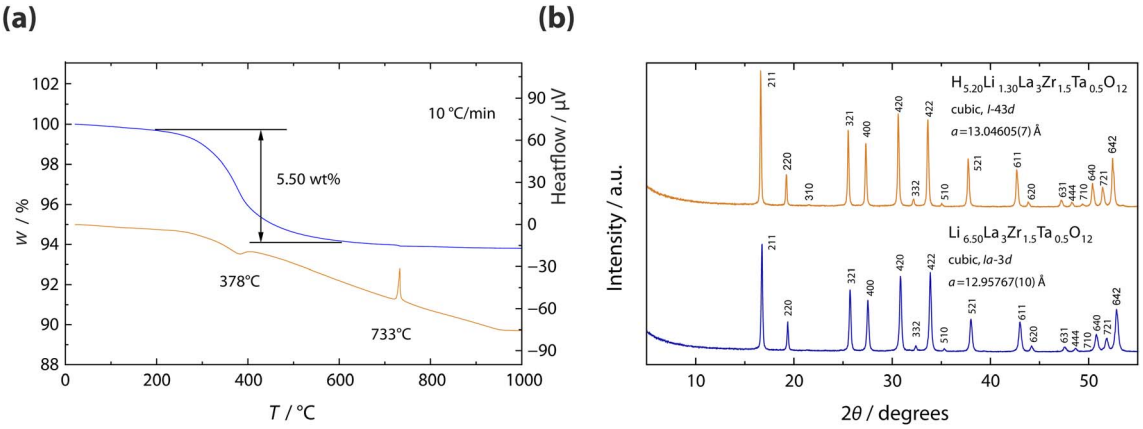

Fig. 2 (a) TG-DTA results of $H_{5.20}Li_{1.30}La_3Zr_{1.5}Ta_{0.5}O_{12}$. (b) XRD patterns of the parent $Li_{6.5}La_3Zr_{1.5}Ta_{0.5}O_{12}$ and the proton-exchanged $H_{5.20}Li_{1.30}La_3Zr_{1.5}Ta_{0.5}O_{12}$ samples. Miller indices (*hkl*) are indicated for the reflections, and the corresponding space groups are also shown.

appearance of this peak suggests a lowering of the crystal symmetry from *Ia*-3*d* to *I*-43*d*, consistent with previous reports for $H_{1.74}Li_{3.59}La_{2.93}Zr_{1.05}Ta_{0.95}O_{12}$.[34]

Local structures of LLZTO and HLZTO

To probe subtle local differences in the proton and lithium substructures of HLZTO and LLZTO, we recorded ^{1}H and ^{6}Li MAS NMR spectra, shown in Fig. 3. In Fig. 3c ^{6}Li MAS spectra are shown before and after the NMR SLR measurements at elevated temperatures, which will be discussed below. The ^{1}H NMR spectra of both samples (see Fig. 3b) exhibit a strikingly broad line (>80 kHz), attributed to protons from the small Vespel caps of the MAS rotors. To confirm the contribution from the rotor material, a rotor was filled with dried $Li_{1.3}Al_{0.3}Ti_{1.7}(PO_4)_3$,[35] which was assumed to be proton-free. In HLZTO, the ^{1}H signal is slightly anisotropic, with a maximum at 2 ppm (referenced to the ^{1}H NMR signal of adamantane, $C_{10}H_{16}$). As first-order chemical shift anisotropies vanish under sufficiently fast MAS conditions, the observed asymmetry likely reflects a convolution of multiple contributions, including the Vespel signal. Interestingly, the ^{1}H spectrum of LLZTO differs from that of proton-free LATP, suggesting that LLZTO can rapidly absorb moisture at least involving the surface regions. The LLZTO signal comprises two lines: one at 2.7 ppm, resembling the main line of HLZTO, and another at −3.2 ppm, absent in HLZTO. A similar lineshape was previously reported by Larraz *et al.* for supposedly dry tetragonal $Li_7La_3Zr_2O_{12}$.[15]

In contrast, the ^{6}Li MAS spectra of LLZTO and HLZTO (Fig. 3a) each display a single resonance. The main line in LLZTO appears at approximately 1 ppm, whereas in HLZTO it is shifted to around 0.3 ppm, reflecting the modified chemical environment induced by protonation. Additionally, the signal intensity in HLZTO is significantly lower, consistent with the reduced lithium content, and the width is also narrower, indicating much weaker dipole-dipole interactions due to the increased Li–Li interatomic distances.

Fig. 3d compares the Raman spectra of LLZTO and HLZTO. The band between 80 and 130 cm^{-1} is dominated by vibrations of the LaO_8 units and is clearly observed in both spectra.[15,36] Contributions from Li–O vibrations are expected in the 200 to 500 cm^{-1} range, which can be further divided into modes of LiO_6 (200 to 300 cm^{-1}) and LiO_4 (350 to 500 cm^{-1}).[37,38] Bands at approximately 653 cm^{-1} and 732 cm^{-1} correspond to the stretching vibrations of the ZrO_6 octahedra and Ta–O units, respectively. While the bands associated with La, Zr, and Ta are very similar in LLZTO and HLZTO despite the difference in unit cell parameters, the Li–O vibration bands show more pronounced differences. In particular, the prominent band at 300 cm^{-1} in HLZTO indicates modifications within the lithium substructure. Both samples also exhibit a relatively small band around 1090 cm^{-1}, characteristic of trace amounts of Li_2CO_3.[38,39]

Conductivity measurements

To probe macroscopic ion transport in HLZTO and LLZTO, conductivity was measured over a broad temperature range. Because the conductivity of HLZTO was significantly lower than that of LLZTO, measurements focused on temperatures above room temperature. The ionic DC conductivity (Fig. 4a), σ_{DC}, was extracted from conductivity isotherms (Fig. S3), obtained by plotting the real part of the conductivity, σ', *versus* frequency, ν. Above 120 °C, a shallow plateau emerges at low frequencies. The corresponding electrical capacitance C of $\sim 10^{-10}$ F indicates a grain boundary process rather than electrode polarization. At higher frequencies, a second, less pronounced plateau corresponds to the bulk process, with a capacitance C of approximately 3×10^{-12} F.

Heating HLZTO to 260 °C (1st run) slightly reduces conductivity, as seen in the Arrhenius plot (Fig. 4a) showing $\sigma_{DC}T = f(1/T)$; the data referring to the cooling run shows slightly lower conductivities at temperatures lower than 100 °C. This effect is more pronounced for the grain-boundary conductivity, suggesting that heating combined with drying, without additional compression, deteriorates the electrical contact between grains. Activation energies are rather high, reaching values of 0.83 and 0.92 eV.

To emphasise bulk properties more clearly, the corresponding electric modulus M was analysed (Fig. 4b). The

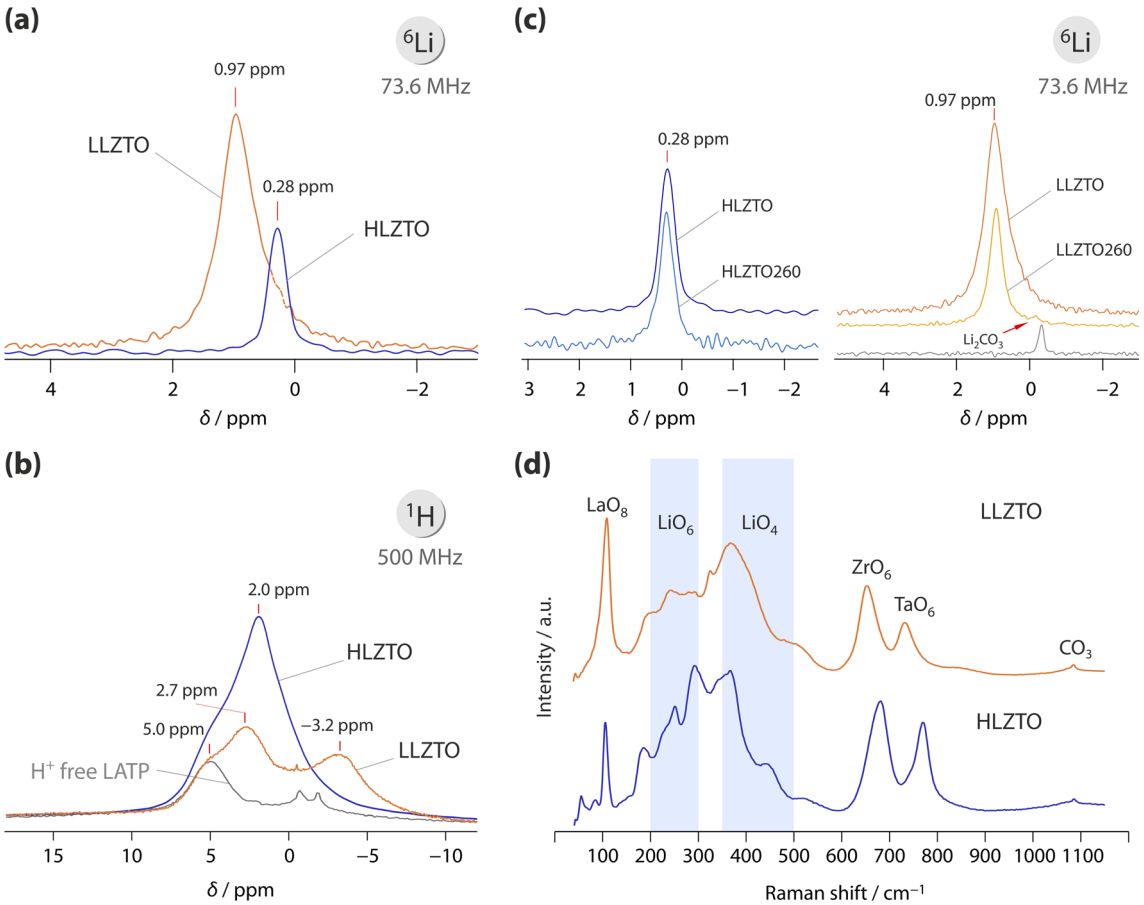

Fig. 3 (a) ^{6}Li MAS NMR spectra (73.6 MHz) of LLZTO and HLZTO, showing a pronounced difference in chemical shift that reflects distinct local Li environments. (b) ^{1}H NMR spectra (500 MHz, 22 kHz spinning speed) of HLZTO, LLZTO, and dried, proton-free LATP, included to illustrate the background ^{1}H signal from the small Vespel rotor caps. Despite protection from moisture, LLZTO exhibits ^{1}H NMR signals, indicating the presence of protons at least on the particle surfaces and in regions slightly beneath the surface. Chemical shifts are referenced to adamantane, see text. (c) ^{6}Li MAS NMR spectra (25 kHz) of HLZTO (a) and LLZTO (b) before and after heating in the static NMR experiment (see below). In HLZTO, the Li NMR signal remains unchanged, whereas in LLZTO, the line becomes significantly narrower, reflecting defect healing. Additionally, a smaller signal appears at −0.3 ppm, likely originating from Li_2CO_3. (d) Raman spectra of LLZTO and HLZTO, with bands characteristic of LiO_6 and LiO_4 highlighted in blue.

imaginary part of the electric modulus, M'', exhibits a maximum at a frequency ν_{max} that corresponds to the characteristic electrical relaxation rate, $\tau_\sigma^{-1} \approx 2\pi\nu_{max}$.[40] Because M is inversely proportional to the electrical capacitance C, the quantity M'' is particularly sensitive to bulk processes, which typically have capacitances *ca.* 2 orders of magnitude smaller than grain boundary processes.[41] Arrhenius plots derived from these hopping rates[42] show no difference between heating and cooling cycles in HLZTO, indicating that temperature primarily affects grain boundary conductivity rather than bulk ion transport, which again is to be characterized by a rather higher activation energy of 0.88 eV, see Fig. 4b.

In most oxides, conductivity is strongly limited by blocking grain boundaries, a phenomenon particularly pronounced in garnets.[43–45] To probe macroscopic diffusion, high-temperature sintering (~1000 °C) is typically required. However, TGA measurements of HLZTO (Fig. 2a) reveal significant mass loss starting around 200 °C, due to the removal of incorporated protons as water.[43] Consequently, higher temperatures cannot be applied to enhance proton conductivity in HLZTO.

In contrast, an LLZTO pellet was annealed *ex situ* at 500 °C for several hours in an argon atmosphere (LLZTO500), resulting in a four-order-of-magnitude higher bulk conductivity; the corresponding conductivity isotherms are shown in Fig. S3. This treatment also allowed clear separation of bulk (~2×10^{-12} F) and grain boundary (~4×10^{-11} F) contributions at temperatures below 60 °C, as illustrated in Fig. 5. The bulk conductivity of LLZTO is characterised by a much lower activation energy of 0.4 eV compared with that of HLZTO. Furthermore, a high-temperature setup was employed to track conductivity changes at elevated temperatures using a non-annealed sample, see Fig. 5. After a first heating cycle to only 300 °C, the overall conductivity increased markedly, even though sintering effects are generally not expected at such low temperatures. This observation is consistent with reports by Akimoto *et al.*, who demonstrated that LLZTO pellets can be successfully sintered by hot pressing at 400 °C.[29]

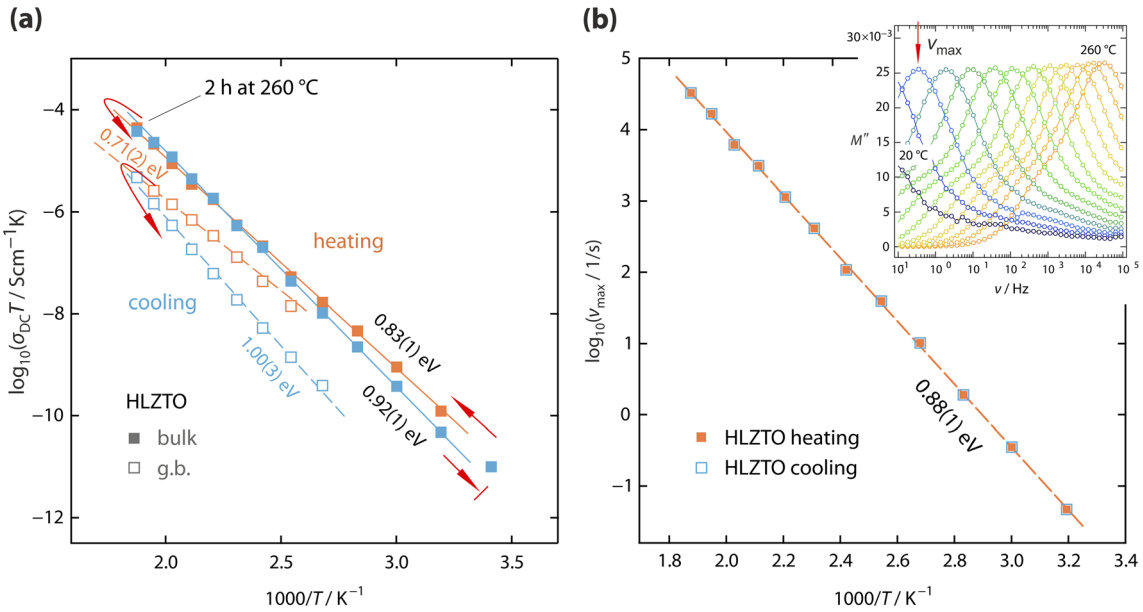

Fig. 4 (a) Arrhenius diagram of bulk and grain boundary DC conductivities of HLZTO during heating from room temperature to 260 °C. Above 120 °C, a second process appears, attributed to grain boundaries (empty symbols). The sample was held at 260 °C for two hours. During cooling, the conductivity decreases more rapidly (blue symbols), particularly the apparent grain boundary contribution. (b) Arrhenius plot of the peak frequencies obtained from the imaginary part of the electric modulus (M'', inset) during heating and cooling. The main peak of M'' originates from electrical bulk relaxation; the peaks shown cover the temperature range from 20 °C to 260 °C.

In a second heating run up to 600 °C, sintering effects become more pronounced. Between 300 °C and 480 °C, the conductivity increases more gradually than below 300 °C (Fig. 5a; see also the magnification in Fig. 5b). A simple explanation might be a phase transition; however, temperature-dependent XRD measurements in this range show no change in the cubic garnet structure. We therefore attribute the slower increase to the healing of defects that enhance Li-ion conductivity, resulting in a reduced activation energy. Above 480 °C, the conductivity rises more rapidly. Upon cooling, the overall

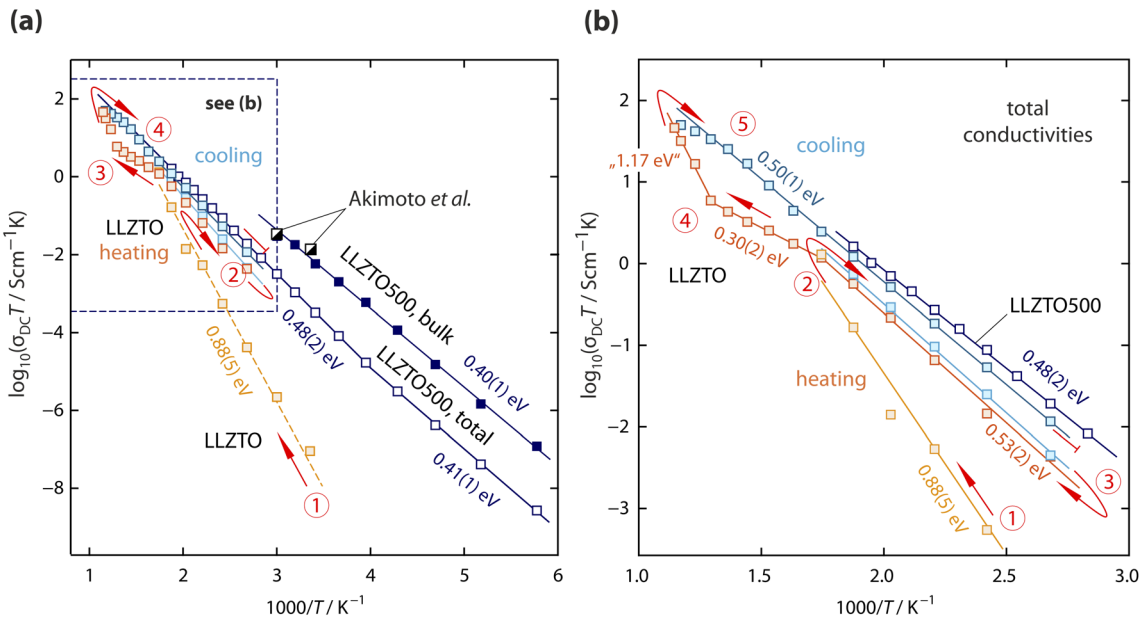

Fig. 5 (a) Arrhenius diagram showing the evolution of the DC conductivities (plotted as $\sigma_{DC}T$) of (non-annealed, cold-pressed) LLZTO and *ex situ*-annealed LLZTO500. LLZTO data were recorded using the high-temperature setup in a first heating run (I) to 300 °C, followed by a second heating run (II) to 600 °C, with 40 °C heating/cooling steps. LLZTO500 data were measured on the standard low-temperature setup between −100 °C and 260 °C, using 20 °C steps. Bulk conductivity for LLZTO (dark blue) could be extracted and is consistent with previous reports by Akimoto *et al.*[29] at 20 °C and 60 °C on pellets obtained by low-temperature sintering. (b) Magnified view of the high-temperature region; numbers indicate the sequential temperature profile during heating and cooling, as also indicated in (b).

conductivity remains higher by roughly half an order of magnitude, indicating improved macroscopic transport with an activation energy of 0.48(2) eV. After *in situ* annealing, the total conductivity at ambient temperature, affected by blocking grain boundaries, is comparable to that of LLZTO (10^{-6} S cm^{-1}). The corresponding bulk conductivity of LLZTO500 (2×10^{-5} S cm^{-1} at 20 °C, 0.40 eV), measurable only for the *ex situ*-annealed pellet, agrees well with previously reported values.[29] The strong agreement between the present data and earlier results on sintered pellets[29] demonstrates that our study successfully probes bulk properties in cold-pressed samples.

^{1}H nuclear spin relaxation

To probe local and long-range H^+ ion transport energy barriers, we performed NMR SLR measurements (Fig. 6). This technique monitors the time-resolved recovery of the longitudinal spin magnetization along the laboratory z-axis. Initially, a series of $\pi/2$ pulses flips the macroscopic magnetization M, originally aligned with the external magnetic field B_0, into the (xy)-plane, where it is rapidly dephased due to fast spin–spin relaxation. The subsequent recovery back along the z-axis, known as nuclear spin relaxation, is recorded *via* time-shifted $\pi/2$ reading pulse to obtain the magnetization transient M_z (Fig. S4). The inflection point of this transient defines the relaxation time T_1, and the relaxation rate, $R_1 \equiv 1/T_1$, is temperature-dependent for the diffusing nuclei. Here, we analysed the transients with stretched exponential functions (see above) to precisely determine the rates. According to the Bloembergen-Purcell-Pound (BPP) model, R_1 is proportional to the spectral density function $J(\omega_0)$, which is the Fourier transform of the motional correlation function G that contains the motional correlation rate τ_c^{-1}.[46] A detailed discussion is provided elsewhere.[32] The temperature dependence of $1/\tau_c$ is assumed to follow an Arrhenius law, $\tau_c^{-1} = \tau_{c0}^{-1}\exp[-E_a/(k_B T)]$, and approximates the ionic jump rate, τ^{-1}, within a factor of two.

In the low-temperature regime ($\omega_0\tau \gg 1$), the relaxation rates increase with temperature. At a characteristic temperature T_{max}, the rate reaches a maximum when ω_0 approaches the jump rate τ^{-1}. At higher temperatures ($\omega_0\tau \ll 1$), the rates decrease, forming the high-temperature flank of the diffusion-induced relaxation rate peak.

In Fig. 6a, the relaxation rates of HLZTO (blue data points) are compared with those from our previous study on a single-crystalline garnet treated in glacial acetic acid (gaa:LLZTO, grey). For both the single crystal and the polycrystalline powder, the R_1 data exhibit only the low-temperature flank, reflecting short-range proton dynamics possibly governed by very low activation energies as low as 0.13 eV. In the present case, the high-temperature flank, which would provide the activation energy for long-range ion transport, could not be accessed because such measurements would require significantly higher temperatures, at which the material is no longer stable (see below).

In many three-dimensional materials, this limitation can be overcome by determining the relaxation rate in the rotating

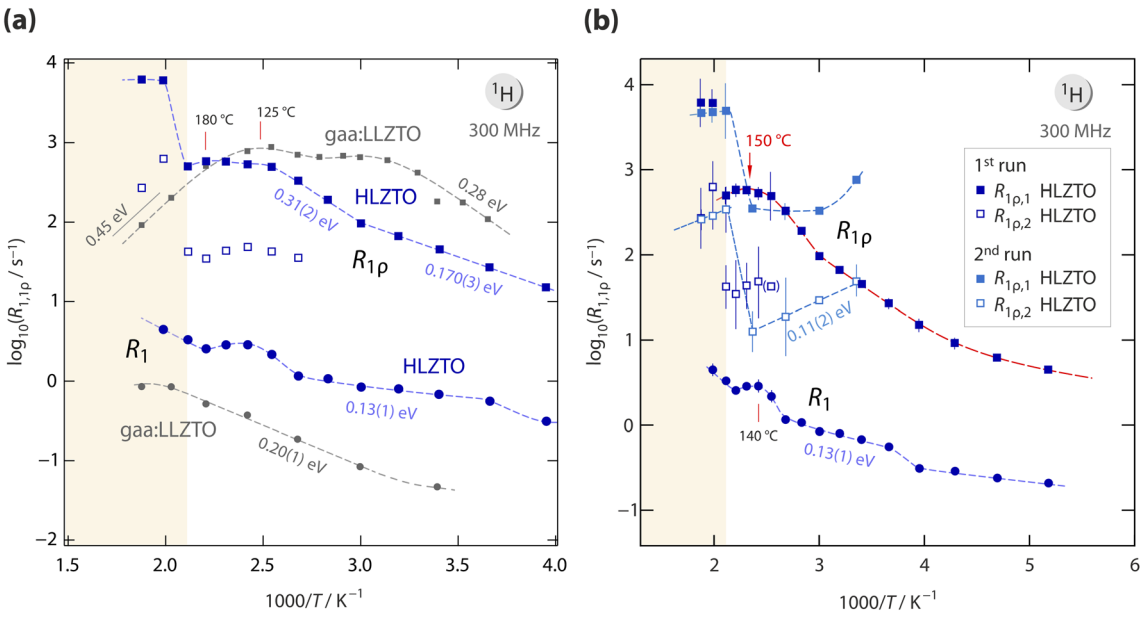

Fig. 6 (a) ^{1}H NMR R_1 and $R_{1\rho}$ relaxation rates of HLZTO (blue) compared with those of single-crystalline gaa:LLZTO (grey), which underwent partial Li/H exchange in glacial acetic acid (gaa), see Gombotz *et al.*[19] In gaa:LLZTO, two distinct maxima appear in the $T_{1\rho}$ data: the low-temperature peak arises from proton-lithium spin interactions, while the second is attributed to proton diffusion. In polycrystalline HLZTO, $R_{1\rho}$ shows a broad maximum between 120 °C and 180 °C. Starting at 80 °C, the transients become double exponential, yielding two distinct rates (filled and open squares). The T_1 relaxation rates of gaa:LLZTO display only the low-temperature flank of a peak, whereas HLZTO shows a local maximum at 150 °C, superimposed by a strong background signal, see also (b). (b) ^{1}H NMR R_1 and $R_{1\rho}$ rates of HLZTO probed over an extended temperature range, comparing the first and second heating runs. Error bars are shown for the $R_{1\rho}$ values; larger uncertainties occur where transients become double exponential. After heating HLZTO above 200 °C, the relaxation rates change significantly, indicating irreversible modification of the sample.

frame of reference using the spin-lock technique.[32] In this approach, the external magnetic field B_0 is effectively replaced by the locking field B_1, which maintains magnetization in the $(xy)'$-plane. This allows the characterization of slower dynamic processes in the kHz regime within a suitable temperature window. The condition for the relaxation-rate maximum, $1/T_{1\rho}$ ($\equiv R_{1\rho}$), is given by $\omega_1\tau \approx 0.5$ where ω_1 is the angular locking frequency corresponding to B_1. Consequently, the maximum shifts toward lower temperatures, making the high-temperature flank accessible. For systems exhibiting three-dimensional diffusion, this flank coincides with that of T_1, as shown, for example, for $Li_6La_3ZrTaO_{12}$ by Stanje *et al.*[47]

Although the ^{1}H NMR R_1 rates of HLZTO and gaa:LLZTO both reveal only the low-temperature flank, subtle differences exist. While gaa:LLZTO exhibits a gradual rise leading to a broad maximum at higher temperatures, HLZTO shows a distinct, but very shallow, local maximum around 140 °C (see also Fig. 6b), followed by another increase in R_1. This behaviour suggests the presence of multiple overlapping dynamic processes, with the high-temperature feature above 200 °C likely related to the release of protons as water molecules. If the local maximum at 140 °C indeed arises from diffusion, it would correspond to rapid proton jumps with rates on the order of 1.9×10^9 s^{-1}.

Comparison of the $R_{1\rho}$ NMR data between HLZTO and gaa:LLZTO provides further insight. The gaa:LLZTO sample exhibits two overlapping rate maxima: the first, at about 60 °C, corresponds to a relatively fast process that cannot be attributed to proton diffusion. We therefore assign it to proton spin fluctuations induced by the rapid motion of lithium ions in gaa:LLZTO, as discussed elsewhere.[19] Proton diffusion becomes evident only at higher temperatures, around 125 °C, as indicated by the second ^{1}H NMR rate peak.[19]

In the strongly protonated HLZTO, this first rate peak is absent, clearly indicating that fast lithium diffusion does not occur. Instead, the relaxation rates increase gradually with temperature (0.17 eV), then more steeply above 60 °C (0.31 eV), reaching a broad maximum between 120 °C and 180 °C, which likely reflects two overlapping relaxation processes. From the maximum condition $\omega_1\tau \approx 0.5$ and the locking field frequency ($\omega_1/2\pi = 20$ kHz), a proton jump rate $\tau^{-1} = 2.5 \times 10^5$ s^{-1} is obtained for the $R_{1\rho}$ maxima. Using the Einstein–Smoluchowski relation and assuming a jump distance of 1.7 Å between tetrahedral and octahedral Li sites for three-dimensional diffusion, this corresponds to an NMR self-diffusion coefficient $D_{NMR,H} = 1.2 \times 10^{-15}$ m^2 s^{-1}. Around 150 °C, this describes a process of similar magnitude to that in the single crystal, while in HLZTO this faster motion is superimposed by a second, slower process reaching comparable diffusivity only near 180 °C.

As $R_{1\rho}$ decreases again above 180 °C, both processes likely contribute to both short-range dynamics and partly long-range ion transport. Activation energies for short-range ion dynamics are considerably lower (0.17 eV, 0.31 eV) than those seen in conductivity spectroscopy for bulk ion transport (*ca.* 0.88 eV, see above). Capturing the high-temperature flank, which would provide detailed information on long-range ion transport, was hindered by a sudden, pronounced rate increase, probably caused by the decomposition of the sample. This decomposition irreversibly alters proton dynamics, as is also evident from the second heating run (Fig. 6b). Interestingly, this abrupt rate change reappears reproducibly in the second run, reminiscent of a phase transition. Although no distinct signal was detected in the DTA (Fig. 2), TGA measurements revealed a marked mass loss beginning at about 200 °C. Adding to the complexity, the magnetization transients become double-exponential above 80 °C (Fig. S4), likely reflecting the coexistence of two relaxation processes with distinct characteristic timescales.

To compare the NMR-derived diffusion parameters with those obtained from conductivity spectroscopy, we applied the Nernst–Einstein relation.[48] Owing to the extremely low conductivities, this yielded a solid-state diffusion coefficient of $D_\sigma = 3.8 \times 10^{-18}$ m^2 s^{-1} at 180 °C. For comparison, Fleig and co-workers reported a bulk interdiffusion coefficient of 7×10^{-17} m^2 s^{-1} at 80 °C,[24] while Kilner and co-workers obtained approximately 10^{-16} m^2 s^{-1} at 100 °C for proton-exchanged, Ga-substituted single-crystalline $Li_7La_3Zr_2O_{12}$.[25] Both literature values are in reasonable agreement with the NMR self-diffusion coefficient ($D_{NMR,H} = 1.2 \times 10^{-15}$ m^2 s^{-1} at *ca.* 150 °C) determined here at somewhat higher temperature. The comparison suggests, however, that the conductivities measured for HLZTO under dry nitrogen are likely underestimated, most probably due to reduced interparticle contact.

Static ^{1}H NMR line measurements

Simultaneously with the NMR SLR experiments, we recorded static ^{1}H NMR spectra of HLZTO over the same temperature range (Fig. 7). Covering such a broad range allows the detection of structural changes that may occur during the SLR measurements and provides additional insight into the dynamic behaviour of the nuclei. For mobile nuclei, the width of the resonance line typically decreases with increasing temperature, an effect commonly known as motional narrowing.[49]

Fig. 7a shows the complete ^{1}H NMR spectrum of HLZTO, while Fig. 7b presents a magnified view of the sharper line at the centre of gravity. Because the ^{1}H nucleus has spin $I = 1/2$, no quadrupolar interactions are expected, and the observed line broadening therefore arises solely from dipolar interactions. From Fig. 7a, it is seen that the two broad components gradually diminish with increasing temperature and disappear entirely above 200 °C. These broad signals, representing the majority of the ^{1}H spins in HLZTO, indicate strong homonuclear dipolar couplings between protons, which weaken significantly as proton mobility increases. The requirement for high temperatures to significantly narrow these spectral features is consistent with the relatively poor H^+ transport properties observed in conductivity spectroscopy.

As shown in Fig. 7b, the much sharper line near the spectral centre of gravity is composed of at least three distinct components. Because these contributions strongly overlap, it is not possible to precisely determine the temperature interval in which the overall motional narrowing sets in. However, the data clearly show that a small fraction of protons accesses multiple

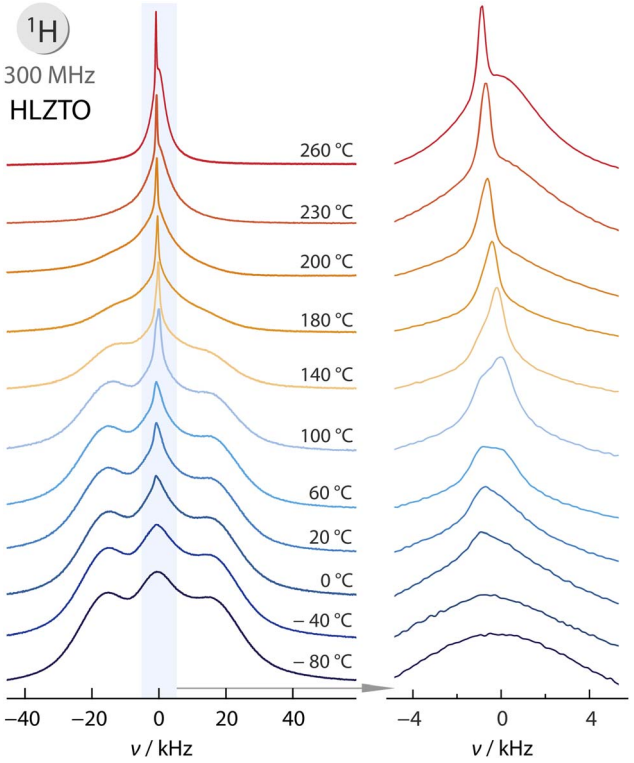

Fig. 7 Static ^{1}H (spin quantum number $I = 1/2$) NMR spectra of H-rich HLZTO recorded at the indicated temperatures and at 300 MHz, that is, using the spectrometer for variable-temperature NMR studies. (Left) Full spectra including the broad background contributions. (Right) Magnified view of the central region highlighting the evolution of a narrow ^{1}H NMR signal arising from proton mobility that is sufficiently fast on the NMR timescale.

diffusion pathways, leading to a stepwise change in the overall ^{1}H NMR spectrum. Most protons, however, are represented by the two very broad spectral components shown in Fig. 7a.

^{7}Li NMR SLR measurements

Protonation of garnets slightly impedes lithium diffusion, even when only a small fraction of Li ions is replaced by protons, as demonstrated previously in our single-crystal NMR relaxation study.[19] To assess the extent of this effect in the present samples, we measured ^{7}Li NMR SLR rates in both the laboratory and rotating frames for HLZTO and LLZTO (Fig. 8). In HLZTO, both rates R_1 and $R_{1\rho}$ are shifted markedly toward higher temperatures compared with LLZTO. Consequently, no distinct rate maximum is visible in $R_{1\rho}$ up to 270 °C, indicating that lithium ions undergo only restricted, localised jumps within the observed temperature range. These jumps are characterized by activation energies of *ca.* 0.27 eV, which determine the slopes of the corresponding low-temperature flanks (Fig. 8).

In contrast, in H-free LLZTO shows a much earlier increase of R_1 and $R_{1\rho}$, reflecting faster ionic motion. Again, the flanks indicate relatively low activation energies ranging from 0.30 to 0.34 eV. The value of 0.34 eV is relatively close to that suggested by bulk conductivity measurements (*ca.* 0.4 eV, Fig. 5a). Around −20 °C, the $R_{1\rho}$ transients become double-exponential; between

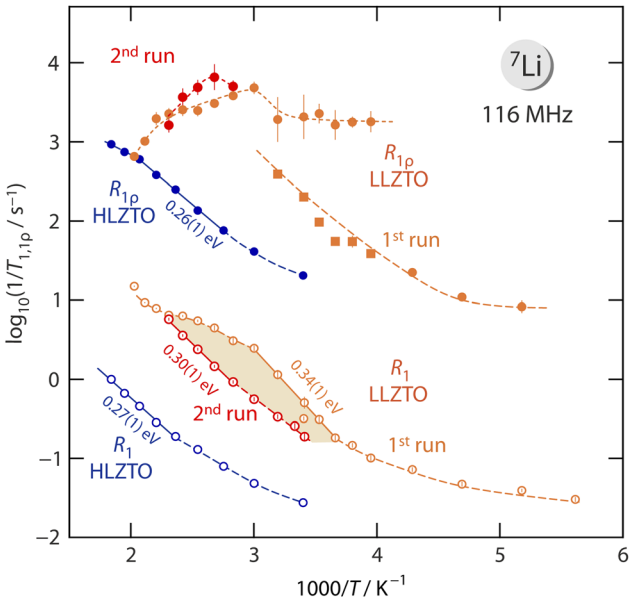

Fig. 8 Comparison of ^{7}Li NMR SLR rates of LLZTO (orange) and HLZTO (blue). Both R_1 and $R_{1\rho}$ indicate that Li^+ diffusion is strongly suppressed in HLZTO. In H-free LLZTO, the relaxation maxima are not directly observable due to concurrent changes in the local defect structure at elevated temperatures, as revealed in a second heating run. Activation energies, extracted from linear fits (continuous lines) of the flank regions, are indicated. The value of 0.34 eV observed for LLZTO agrees with the activation energy determined for bulk ion dynamics *via* conductivity spectroscopy.

−10 and 20 °C, both components contribute equally to the total magnetization (see Fig. S4). A discontinuity in $R_{1\rho}$ is observed near 330 K. For comparison, in single-crystalline LLZTO, NMR relaxation shows a maximum already at 185 K.[47] This shift is consistent with the lower conductivity of our polycrystalline LLZTO, which is inferior to that of highly sintered[36,50,51] or single-crystalline garnets that reach conductivities in the mS range at ambient conditions.[26,52]

At lower temperatures, R_1 of LLZTO increases only gradually, signifying ionic motion with a low activation barrier or relaxation due to non-diffusive effects. Above −20 °C, the rates rise more steeply, marking the onset of a diffusion-induced relaxation peak with a flank yielding to 0.34 eV, a value being consistent with bulk conductivity measurements (see above). Beyond roughly 60 °C, however, the increase slows, producing a kink along the low-temperature flank. Even after heating to higher temperatures, a distinct rate maximum did not develop. After cooling and re-measuring in a second heating run, the relaxation rates were significantly reduced, revealing diminished localised motion following thermal exposure to approximately 200 °C. The apparent $R_{1\rho}$ maximum also shifted to higher temperatures in this run.

Any discrepancies in activation energies and differences in trends upon annealing, as observed by NMR and conductivity measurements, can be explained by the differing time- and length-scale sensitivities of the two techniques. The low-temperature flank primarily reflects activation barriers of local, short-range Li^+ jumps, which are strongly influenced by

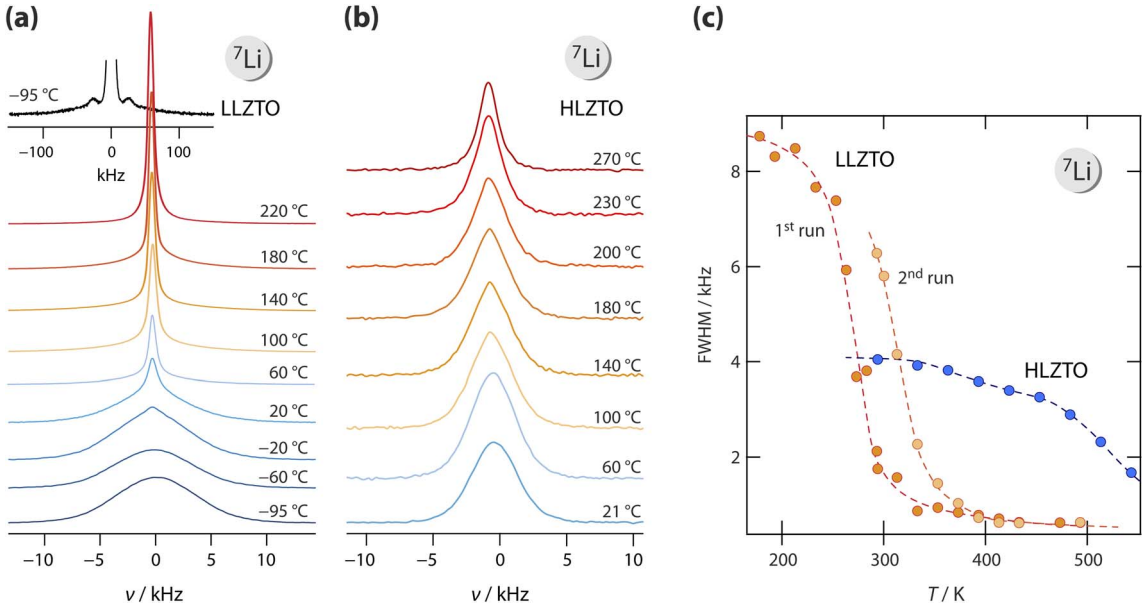

Fig. 9 Static ^{7}Li ($I = 3/2$) NMR lines of (a) LLZTO and (b) HLZTO recorded at the indicated temperatures. The inset in (a) shows the full spectrum including the 90° satellite singularities of the quadrupolar powder pattern pointing to a coupling constant of *ca.* 100 kHz. In (c), the line widths, FWHM (full width at half maximum), are plotted against temperature. The shift of the second run of LLZTO to higher temperatures shows that (local) Li diffusivity was irreversibly decreased after heating. ^{7}Li NMR line narrowing in HLZTO occurs only at much higher temperatures, indicating sluggish Li^+ mobility.

defects such as dislocations and grain boundaries, see, for example, the defect-affected NMR rates of Li_3InCl_6 samples prepared by different methods, as investigated recently.[53] Upon heating, defect healing reduces the number of such extrinsic sites, suppressing localised defect-mediated motion detectable by NMR. At the same time, annealing improves intergranular contact and may also enhance long-range transport pathways within the bulk, thereby enhancing the overall (total) macroscopic conductivity measured by impedance spectroscopy.

Both NMR and conductivity spectroscopy confirm that Li diffusion is strongly suppressed in HLZTO as a result of proton exchange. A straightforward explanation is that the Li diffusion pathways are no longer continuously occupied by Li ions but are largely blocked by protons, which move more slowly due to different binding environments and stronger electrostatic interactions with the host lattice. This behaviour is also reflected in the ^{7}Li NMR line shapes.

^{7}Li NMR line shapes

A consistent picture of Li diffusivity in the two samples emerges from the static ^{7}Li ($I = 3/2$) NMR spectra shown in Fig. 9. The same spectra, shown over the full frequency range to highlight the quadrupolar contributions visible as singularities flanking the central line, are shown in Fig. S5 and for −95 °C in the inset of Fig. 9a. Quadrupolar intensities are more pronounced in LLZTO due to the higher Li concentration; the 90° singularities with a splitting of 50 kHz point to a quadrupolar coupling constant of *ca.* 100 kHz if an axially symmetric electric field gradient at the nuclear Li site is assumed.

Focusing on the central lines shown in Fig. 9a, in H-free LLZTO, the lines begin to narrow around −60 °C, whereas in HLZTO only minor changes in width occur between 20 °C and 200 °C (Fig. 9b), followed by a more pronounced narrowing step above 180 °C. Such clear changes undouble reveal much slower Li^+ ions in H-rich HLZTO. In Fig. 9c, we plotted the line widths (full width at half maximum, FWHM) of the static ^{7}Li NMR signals as a function of temperature. It is evident that Li spins in LLZTO diffuse clearly faster on the NMR timescale compared to those in HLZTO. This significant difference is apparent because motional line narrowing in LLZTO (first run) sets in at much lower temperatures, while the corresponding curve for HLZTO is shifted to higher temperatures. The pronounced reduction in Li conductivity inferred from NMR line narrowing is consistent with the decreased Li^+ mobility observed in SLR NMR (Fig. 8). Because NMR probes bulk ion dynamics and is largely independent of pellet densification or sintering quality, the lower conductivity observed for HLZTO (see Fig. 4a) cannot be attributed solely to insufficient sintering of the corresponding pellets. The overall decrease in Li^+ is clearly seen in NMR measurements and largely contributes to the much lower overall (ionic, Li^+ and H^+) conductivity in HLZTO.

In a second run, we observe that the ^{7}Li NMR motional narrowing curve for LLZTO shifts toward higher temperatures, indicating reduced Li^+ diffusivity after soft annealing. Assuming that NMR lines are influenced not only by averaging of dipolar interactions through long-range ion dynamics but also, to some extent, by localized motions triggered by point defects, this behavior mirrors the changes seen in the R_1 NMR rates (see the discussion above and Fig. 8). We propose that defect healing suppresses short-range (localized) hopping while enhancing through-going (long-range) ion transport in the studied compounds as is finally probed in conductivity spectroscopy (see Fig. 5b).

Structural changes of HLZTO as seen by NMR and XRD

To assess structural changes in HLZTO upon exposure to high temperatures, high-temperature XRD measurements up to 300 °C show only a slight contraction of the lattice parameter (Fig. S6), which is consistent with proton removal in the form of H_2O. The accompanying loss of oxygen may further contract the lattice through deformation of the Zr/TaO_6 octahedra. Hence, the slight change in linewidth below 180 °C (see Fig. 7) may be attributed to the structural modifications observed in the XRD data described above. In contrast, the local environment of the remaining Li ions remains largely unaffected, as evidenced by the ^{6}Li MAS NMR spectra of the powder used in the NMR SLR experiments (see Fig. 3c). Similarly, ^{6}Li MAS NMR of H-free LLZTO after the SLR measurements shows a significant line narrowing, indicating faster Li dynamics, and a small additional signal at approximately −0.3 ppm, consistent with minor lithium carbonate formation.

Consistent with trends observed recently,[19] Li diffusivity is slowed in Li–H exchanged garnet samples. Proton mobility is observable in these samples, with moderate diffusion coefficients as discussed above. Additionally, ^{1}H NMR SLR measurements indicate fast localised proton motion, which, however, does not significantly contribute to long-range H transport in HLZTO.

Conclusion

We studied proton dynamics in Li–H exchanged garnets, selecting LLZTO as a model system to quantify jump rates, diffusion coefficients, and activation energies governing proton mobility in these oxides. Starting from lithium-rich LLZTO, the garnet structure is retained even when most lithium ions are replaced by protons. ICP-OES and ^{6}Li MAS NMR measurements show that a small fraction of the original lithium remains after the Li/H exchange reaction reaches completion, as indicated by a stable pH. Raman spectra confirm the presence of lithium within the garnet lattice, in addition to the characteristic vibrations of LaO_8, ZrO_6, and TaO_6 units. The fine sub-micrometer particle morphology facilitates efficient proton exchange and contributes to the observed dynamics.

Conductivity spectroscopy combined with element-specific NMR reveals that the remaining lithium ions are largely immobilised, making protons the dominant charge carriers. Although long-range proton transport is impeded by grain boundary resistance, relatively fast proton dynamics are observed *via* ^{1}H NMR SLR measurements. Several dynamic processes overlap within the studied temperature range, with a broad maximum between 120 and 180 °C, suggesting the onset of long-range bulk proton diffusion, characterised by a self-diffusion coefficient of $D_{NMR,H} = 1.2 \times 10^{-15}$ m^2 s^{-1} at approximately 150 °C. In contrast, lithium motion remains highly restricted under the same conditions.

In LLZTO, conductivity can be enhanced by moderate thermal treatment (~300 °C), which reduces grain boundary resistance. However, NMR shows that localised ionic motion, driven by extrinsic defects, diminishes after heating above 200 °C. In HLZTO, excessive thermal treatment leads to proton loss, impairing both intergrain conductivity and likely localised bulk diffusion. Overall, these results highlight NMR as a powerful tool for probing bulk diffusion processes and resolving local ionic dynamics in proton-conducting garnets, with implications for the design of solid electrolytes where proton mobility dominates over lithium transport.

Author contributions

F. S. performed the NMR and conductivity measurements, contributed to conceptualization, and prepared the manuscript. J. A. was responsible for sample preparation, characterization, and data analysis. Y. M. carried out the TG-DTA and structural analyses. K. M. conducted the SEM and TEM analyses. K. T. contributed to sample preparation and scientific discussion. H. M. R. W. contributed to conceptualization, manuscript preparation, scientific discussion, and supervised the project.

Conflicts of interest

The authors declare that they have no conflicts of interest.

Data availability

All data generated or analysed during this study are included in this published article (and its supplementary information (SI)). Supplementary information is available. See DOI: https://doi.org/10.1039/d5ta09970f.

Acknowledgements

We thank Francesco Carraro and Paolo Falcaro for the Raman measurements. We acknowledge financial support from the DFG (WI3600 2-1 and 4-1), the Japan Society for the Promotion of Science (JSPS) KAKENHI (Grant Number JP24K08593), and the National Institute for Materials Science (NIMS) Battery Research Platform, as well as from the "Advanced Research Infrastructure for Materials and Nanotechnology in Japan (ARIM)" of the Ministry of Education, Culture, Sports, Science and Technology (MEXT), Japan (Proposal Numbers JPMXP1224NM5346 and JPMXP1225NM5365).

References

1 W. Zhang and Y. H. Hu, *Energy Sci. Eng.*, 2021, **9**, 984–1011.
2 H. Iwahara, *Solid State Ionics*, 1996, **86–88**, 9–15.
3 H. Iwahara, T. Esaka, H. Uchida and N. Maeda, *Solid State Ionics*, 1981, **3–4**, 359–363.
4 T. Norby, *Solid State Ionics*, 1999, **125**, 11.
5 S. Sun, Q. Tang, K. Zhang, Y. Wen, A. Billings and K. Huang, *Mater. Adv.*, 2023, **4**, 389–407.
6 C. Dreßler and D. Sebastiani, *Phys. Chem. Chem. Phys.*, 2020, **22**, 10738–10752.
7 H. P. Rodenburg, F. Stainer, K. M. Draijer, H. Ni, J. Spychala, N. Artrith, H. M. R. Wilkening and P. Ngene, *Adv. Funct. Mater.*, 2024, **35**, 2412219.

8 G. C. Mather and M. S. Islam, *Chem. Mater.*, 2005, **17**, 1736–1744.
9 L. Bi, S. P. Shafi and E. Traversa, *J. Mater. Chem. A*, 2015, **3**, 5815–5819.
10 L. Buannic, L. Sperrin, R. Dervişoğlu, F. Blanc and C. P. Grey, *Phys. Chem. Chem. Phys.*, 2018, **20**, 4317–4328.
11 F. M. Draber, C. Ader, J. P. Arnold, S. Eisele, S. Grieshammer, S. Yamaguchi and M. Martin, *Nat. Mater.*, 2019, **19**, 338–346.
12 S. Barison, M. Battagliarin, S. Boldrini, G. Chiodelli, L. Doubova, M. Fabrizio, R. Gerbasi, L. Malavasi and C. Mortalò, *ECS Transact.*, 2008, **11**, 89.
13 T. Wei, L. A. Zhang, Y. Chen, P. Yang and M. Liu, *Chem. Mater.*, 2017, **29**, 1490–1495.
14 A. Ishii, D. Kume, S. Nakayasu, I. Oikawa, H. Matsumoto, H. Kato and H. Takamura, *Mater. Adv.*, 2024, **5**, 1531–1539.
15 G. Larraz, A. Orera, J. Sanz, I. Sobrados, V. Diez-Gómez and M. L. Sanjuán, *J. Mater. Chem. A*, 2015, **3**, 5683–5691.
16 S. Ohta, M. Kawakami, H. Nozaki, C. Yada, T. Saito and H. Iba, *J. Mater. Chem. A*, 2020, **8**, 8989–8996.
17 C. Galven, J.-L. Fourquet, M.-P. Crosnier-Lopez and F. Le Berre, *Chem. Mater.*, 2011, **23**, 1892–1900.
18 L. Truong and V. Thangadurai, *Inorg. Chem.*, 2012, **51**, 1222–1224.
19 M. Gombotz, C. Hiebl, F. Stainer and H. M. R. Wilkening, *J. Phys. Chem. C*, 2023, **127**, 10960–10967.
20 M. Nyman, T. M. Alam, S. K. McIntyre, G. C. Bleier and D. Ingersoll, *Chem. Mater.*, 2010, **22**, 5401–5410.
21 M. A. Howard, O. Clemens, E. Kendrick, K. S. Knight, D. C. Apperley, P. A. Anderson and P. R. Slater, *Dalton Trans.*, 2012, **41**, 12048–12053.
22 L. Truong, M. Howard, O. Clemens, K. S. Knight, P. R. Slater and V. Thangadurai, *J. Mater. Chem. A*, 2013, **1**, 13469.
23 C. Hiebl, D. Young, R. Wagner, H. M. R. Wilkening, G. J. Redhammer and D. Rettenwander, *J. Phys. Chem. C*, 2018, **123**, 1094–1098.
24 S. Smetaczek, A. Limbeck, V. Zeller, J. Ring, S. Ganschow, D. Rettenwander and J. Fleig, *Mater. Adv.*, 2022, **3**, 8760–8770.
25 R. H. Brugge, R. J. Chater, J. A. Kilner and A. Aguadero, *J. Phys. Energy*, 2021, **3**, 034001.
26 K. Kataoka, *J. Cer. So. Jpn.*, 2020, **128**, 7–18.
27 J. Gu, L. Jiang, S. A. Ismail, H. Guo and D. Han, *Adv. Mater. Interf.*, 2022, **10**, 2201764.
28 J. Akimoto, T. Akao and K. Kataoka, *Small*, 2023, **19**, e2301617.
29 J. Akimoto, T. Akao, H. Nagai and K. Kataoka, *ACS Appl. Mater. Interfaces*, 2023, **15**, 18973–18981.
30 N. Hamao, K. Hamamoto, N. Taguchi, S. Tanaka and J. Akimoto, *Solid State Ionics*, 2020, **357**, 115460.
31 V. Petříček, L. Palatinus, J. Plášil and M. Dušek, *Z. Kristallogr. - Cryst. Mater.*, 2023, **238**, 271–282.
32 V. Epp, Ö. Gün, H. J. Deiseroth and M. Wilkening, *Phys. Chem. Chem. Phys.*, 2013, **15**, 7123.
33 Y. Li, J.-T. Han, S. C. Vogel and C.-A. Wang, *Solid State Ionics*, 2015, **269**, 57–61.
34 G. J. Redhammer, P. Badami, M. Meven, S. Ganschow, S. Berendts, G. Tippelt and D. Rettenwander, *ACS Appl. Mater. Interfaces*, 2021, **13**, 350–359.
35 T. Scheiber, B. Gadermaier, M. Finsgar and H. M. R. Wilkening, *Adv. Funct. Mater.*, 2024, **34**, 2404562.
36 A. Alsawaf, G. Karkera, T. Diemant, M. V. Kante, Y. Schneider, L. Velasco, S. S. Bhattacharya, F. Stainer, M. Wilkening, O. Clemens, J. Janek, H. Hahn and M. Botros, *Small Struct.*, 2025, **6**, 2400643.
37 Y. Luo, Y. Zhang, Q. Zhang, Y. Zheng, H. Chen and L. Guo, *Ceram. Intern.*, 2019, **45**, 17874–17883.
38 E. Enkhbayar and J. Kim, *ACS Omega*, 2022, **7**, 47265–47273.
39 M. Rosen, R. Ye, M. Mann, S. Lobe, M. Finsterbusch, O. Guillon and D. Fattakhova-Rohlfing, *J. Mater. Chem. A*, 2021, **9**, 4831–4840.
40 R. Winter, K. Siegmund and P. Heitjans, *J. Non-Cryst. Solids*, 1997, **212**, 215–224.
41 J. T. S. Irvine, D. C. Sinclair and A. R. West, *Adv. Mater.*, 1990, **2**, 132–138.
42 B. Munro, M. Schrader and P. Heitjans, *Ber. Bunsenges. Phys. Chem.*, 1992, **96**, 1718–1723.
43 J. A. Hammons, J. A. Espitia, E. Ramos, R. Shi, F. Meisenkothen, M. Wood, M. R. Cerón and J. Ye, *J. Mater. Chem. A*, 2022, **10**, 9080–9090.
44 S. Ohta, Y. Kihira and T. Asaoka, *Front. Energy Res.*, 2016, **4**, 30.
45 W. E. Tenhaeff, E. Rangasamy, Y. Wang, A. P. Sokolov, J. Wolfenstine, J. Sakamoto and N. J. Dudney, *Chem. Electro. Chem.*, 2013, **1**, 375–378.
46 N. Bloembergen, E. M. Purcell and R. V. Pound, *Phys. Rev.*, 1948, **73**, 679–712.
47 B. Stanje, D. Rettenwander, S. Breuer, M. Uitz, S. Berendts, M. Lerch, R. Uecker, G. Redhammer, I. Hanzu and M. Wilkening, *Ann. Phys.*, 2017, 529.
48 F. Stainer, B. Gadermaier, A. Kügerl, L. Ladenstein, K. Hogrefe and H. M. R. Wilkening, *Solid State Ionics*, 2023, **395**, 116209.
49 J. R. Hendrickson and P. J. Bray, *J. Magn. Res.*, 1973, **9**, 341–357.
50 D. Rettenwander, G. Redhammer, F. Preishuber-Pflügl, L. Cheng, L. Miara, R. Wagner, A. Welzl, E. Suard, M. M. Doeff, M. Wilkening, J. Fleig and G. Amthauer, *Chem. Mater.*, 2016, **28**, 2384–2392.
51 P. Badami, J. M. Weller, A. Wahab, G. Redhammer, L. Ladenstein, D. Rettenwander, M. Wilkening, C. K. Chan and A. N. M. Kannan, *ACS Appl. Mater. Interfaces*, 2020, **12**, 48580–48590.
52 M. Philipp, B. Gadermaier, P. Posch, I. Hanzu, S. Ganschow, M. Meven, D. Rettenwander, G. J. Redhammer and H. M. R. Wilkening, *Adv. Mater. Interf.*, 2020, **7**, 2000450.
53 F. Stainer, B. Gadermaier and H. M. R. Wilkening, *Chem. Mater.*, 2025, **37**, 2650–2663.